

Measuring Higgs Self-Coupling at CMS

by

Sabrina Gonzalez Pasterski

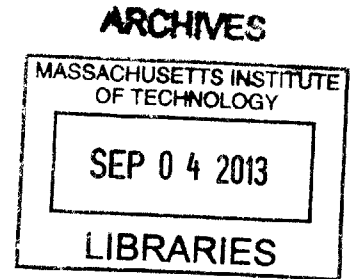
Submitted to the Department of Physics in partial fulfillment of the Requirements
for the Degree of

BACHELOR OF SCIENCE

at the

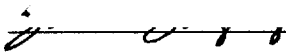
MASSACHUSETTS INSTITUTE OF TECHNOLOGY

June, 2013



© MMXIII SABRINA GONZALEZ PASTERSKI
All Rights Reserved

The author hereby grants to MIT permission to reproduce and to distribute publicly
paper and electronic copies of this thesis document in whole or in part.

Signature of Author:  _____
Department of Physics
May 10, 2013

Certified by: _____
Professor Markus Klute
Thesis Supervisor, Department of Physics

Accepted by: _____
Professor Nergis Mavalvala
Senior Thesis Coordinator, Department of Physics

Measuring Higgs Self-Coupling at CMS

by

Sabrina Gonzalez Pasterski

Submitted to the Department of Physics
in May of 2013 in partial fulfillment of the
requirements for the degree of
Bachelor of Science in Physics

Abstract

This study evaluates the Compact Muon Solenoid (CMS) experiment's ability to characterize Higgs self-coupling through the $gg \rightarrow HH \rightarrow b\bar{b}\tau\bar{\tau}$ channel. The effective cross-section for detecting $gg \rightarrow HH \rightarrow b\bar{b}\tau\bar{\tau}$ events is computed by finding the fraction of simulated events that make it through selection cuts. These same cuts also are applied to simulated background samples. The result is then compared to a recent theoretical study on measuring Higgs self-coupling to check the applicability of its assumptions and the feasibility of its predictions. This study finds that the selection algorithms currently used for $\tau\bar{\tau}$ analyses at CMS produce a lower yield of signal events. Since the $gg \rightarrow HH \rightarrow b\bar{b}\tau\bar{\tau}$ channel was predicted to be one of the most promising for characterizing the Higgs self-coupling constant, λ_{HHH} , the results of this study indicate that, unless the methods for reconstructing detected particles are improved, future data collected by CMS will not be sufficient to complete such an analysis.

Thesis Supervisor: Professor Markus Klute

Acknowledgements

This Thesis builds on work that started as an Undergraduate Research Opportunity in May of 2012. I spent the summer of the Higgs discovery helping to prepare detector components for installation during the 2013-2014 LHC shutdown and working on a preliminary study of how to distinguish particles originating from different vertices when the LHC's instantaneous luminosity increases in the coming decades.

This study begins as a response to: "What's next after we've found the Higgs?", continues with a prediction of what we will find when CERN begins taking data at $\sqrt{s} = 13$ TeV in 2015, and concludes with results that recommend further upgrades in the coming years.

I am grateful to the MIT CMS team that guided me throughout, and fortunate to have arrived at CERN at the dawn of a new era of particle physics.

Contents

1	Introduction	11
1.1	CMS	11
1.2	The Higgs Boson	12
2	Higgs Self-Coupling	15
2.1	The Higgs Mechanism	15
3	Simulating Di-Higgs Production	19
3.1	Cross-sections for Self-Coupling	19
3.2	Simulation Tools	19
4	Decay Channels	23
4.1	Restriction to $HH \rightarrow b\bar{b}\tau\bar{\tau}$	23
4.2	Detected Final States	24
5	Background Processes	25
5.1	ZH Background	25
5.2	$t\bar{t}$ Background	26
5.3	Background Simulation	26
6	Event Selection	29
6.1	Effective Cross-Section	29
6.2	Final State Identification	29
6.3	Kinematical Cuts	30
6.4	Signal vs. Background	31
7	Results	33
7.1	Effective Cross-Section Values	33
7.2	Comparison to Prediction	33
7.3	Evaluating Backgrounds	36
7.4	Comparing Final States	37
8	Conclusions and Future Work	41

List of Figures

1.1	Schematic of a slice through the CMS detector. Image credit: CERN.	12
1.2	Elementary particles of the Standard Model. Image credit: Fermilab.	13
2.1	Higgs potential, visualizing the ring of minima that leads to spontaneous symmetry breaking. Image credit: Nature.	15
2.2	Plot adapted from Ref. [1] of the fractional change in the expected cross-section for di-Higgs production when λ_{HHH} is varied from its Standard Model value λ_{HHH}^{SM}	17
3.1	Combined η and p_T distributions for the two Higgs bosons generated by Madgraph at center of mass energies of 8, 14, and 100 TeV.	20
3.2	Di-Higgs center of mass energy, corresponding to the mass distribution for the off-shell Higgs boson in decays involving Higgs self-coupling.	20
7.1	$M_{\tau\bar{\tau}}$ distribution for events passing selection cuts.	37
7.2	$M_{b\bar{b}}$ distribution for events passing selection cuts.	38
7.3	$M_{\tau\bar{\tau}}$ distribution for events passing selection cuts showing the breakdown between different $\tau\bar{\tau}$ decay channels.	39
7.4	$M_{b\bar{b}}$ distribution for events passing selection cuts showing the breakdown between different $\tau\bar{\tau}$ decay channels.	39

Chapter 1

Introduction

1.1 CMS

The Large Hadron Collider (LHC) is a 27 km circumference particle accelerator located underground at the border between France and Switzerland. It is operated by CERN (the Organisation Européenne pour la Recherche Nucléaire), an international organization for particle physics. At CERN, two main collaborations, CMS and ATLAS, analyze collisions using different equipment. This paper focuses on proton-proton collisions, although heavy ion collisions using lead nuclei are also performed during parts of the year. CMS stands for Compact Muon Solenoid, a large cylindrical magnet packed with particle detectors, as illustrated in Figure 1.1. As protons collide at the center of this cylinder, they are tracked in the inner region and stopped in the outer layers. One can ascertain information, such as the transverse momentum (p_T) and charge of a particle, from the shape of the particle's path. By stopping a particle and measuring the energy it deposited, one can calculate its initial energy.

The Standard Model (SM), summarized in Figure 1.2, predicts how particles will interact with each other. To detect the actual occurrence of these interactions, the final decay products trigger the readout of the detector in a way that distinguishes such interactions from other backgrounds. To gather more precise measurements one must either collect more data or choose a method for selecting data that reduces background events. An evaluation of how well one can measure a certain property of a particle is detector-dependent. This study uses analytical methods CMS currently employs on collected data to evaluate selection efficiencies for simulated data and compare what has been predicted theoretically in Ref. [1] to what CMS could expect to find if sufficient actual data were available.

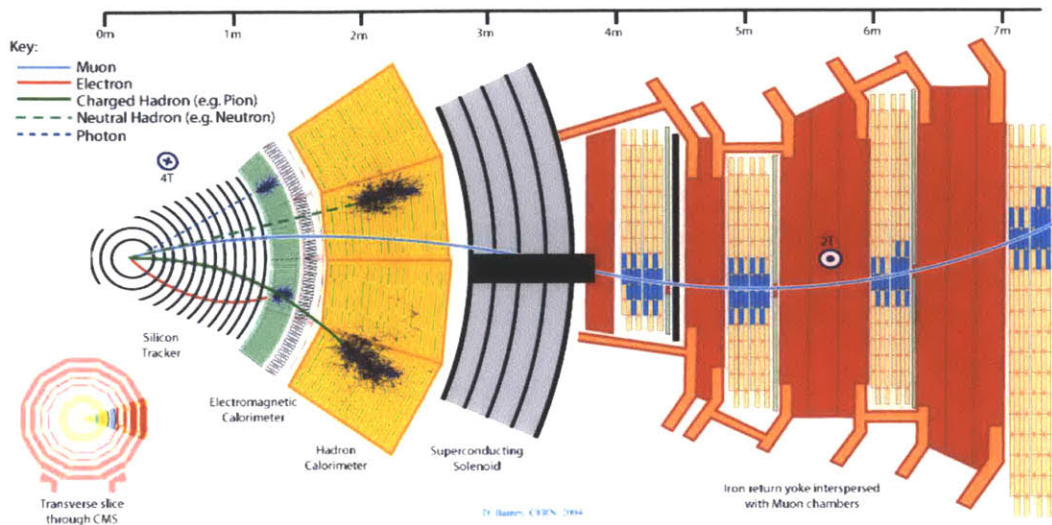


Figure 1.1: Schematic of a slice through the CMS detector. Image credit: CERN.

1.2 The Higgs Boson

The Higgs mechanism describes how the Standard Model's elementary particles acquire mass. It also introduces a new particle, the Higgs boson. While the Higgs boson's mass is not predicted by the Standard Model, its interactions with other particles can be predicted as a function of its mass. After years of searching different mass regimes at CERN's Large Electron-Positron Collider (LEP), Fermilab's Tevatron, and CERN's Large Hadron Collider (built in the former LEP tunnel), CMS and ATLAS on July 4, 2012 announced the discovery of a Higgs-like particle at 125 GeV.

Once the mass of this particle is known, the Standard Model provides an exact expression for the Higgs potential. That potential dictates the strength of self-interactions of the boson. One way to determine if this newly found particle is actually the SM Higgs boson is to study Higgs self-coupling. Namely, look for events where an off-shell Higgs boson (one with a mass is different from the measured mass of 125 GeV) decays into two on-shell Higgs bosons (with masses of 125 GeV).

Finding the Higgs boson was compared to finding a needle in a haystack. Characterizing Higgs self-coupling is like finding the string and threading the needle. To locate self-coupling events, the LHC must produce and detect not one, but two Higgs bosons. Such events are very rare.

The cross-section, which is a measure of how likely a specific process occurs in a proton-proton collision, increases with the center of mass energy of the colliding particles. This paper describes a preliminary study on the ability to characterize

Higgs self-coupling using CMS after an upgrade to the collision energy of the LHC is completed in 2015. This upgrade will increase \sqrt{s} from 8 TeV to 13 TeV. Rare self-coupling events are simulated by the thousands so that kinematical distributions can be analyzed and used to predict good selection cuts for when enough actual data is acquired ten to twenty years from now. The key to determining the feasibility of a self-coupling measurement lies not only in the number of self-coupling events we expect to find in our data, but also in the ability to correctly reconstruct those events and distinguish them from background.

		Model of Elementary Particles						
		Three Generations of Matter (Fermions)			Force Carriers (Gauge Bosons)			
(Name)	Electric Charge							
(Symbol)	Number of Color Charges							
	Mass in MeV							
Q u a r k s	I		II		III			
	Up	+2/3	Charm	+2/3	Top/ Truth	+2/3	Photon	0
	u	3	c	3	t	3	γ	0
		~5		~1350		> 131000		
	Down	-1/3	Strange	-1/3	Bottom/ Beauty	-1/3	Gluon	0
	d	3	s	3	b	3	g	8
	~9		~175		~4500		0	
L e p t o n s	Electron Neutrino	0	Muon Neutrino	0	Tau Neutrino	0	Z zero	0
	ν_e	<.0000070	ν_μ	<.27	ν_τ	<31	Z⁰	91187
	Electron	-1	Muon	-1	Tau	-1	W plus minus	±1
	e	511	μ	105.66	τ	1777.1	W[±]	80220

September 1994

Figure 1.2: Elementary particles of the Standard Model. Image credit: Fermilab.

Chapter 2

Higgs Self-Coupling

2.1 The Higgs Mechanism

The Higgs field is described by complex doublet Φ . With the Higgs mechanism, the Lagrangians that describe SM elementary particles contain an extra potential term that includes this Higgs field. Interactions with the Higgs field give elementary particles their mass. The Higgs potential itself can be written as:

$$V(\Phi) = -\mu^2\Phi^\dagger\Phi + \frac{1}{2}\lambda(\Phi^\dagger\Phi)^2. \quad (2.1)$$

What is special about the Higgs potential is that its minimum does not occur when the field is zero. Instead, a degenerate ring of minima occurs at a radius $r = \sqrt{\mu^2/\lambda}$, as shown in Figure 2.1.

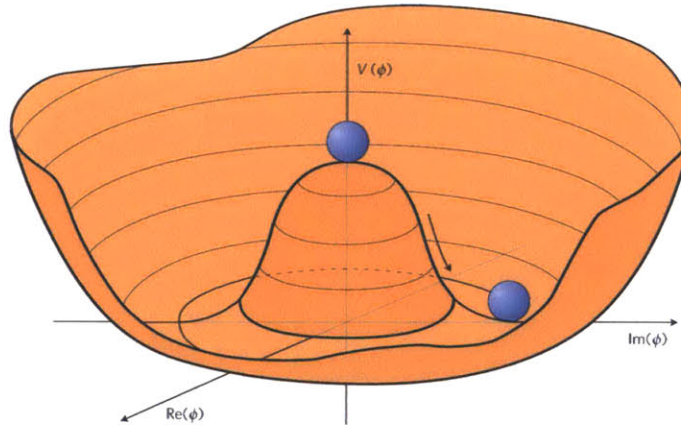


Figure 2.1: Higgs potential, visualizing the ring of minima that leads to spontaneous symmetry breaking. Image credit: Nature.

Spontaneous symmetry breaking refers to the choice we have in selecting the minimum about which to expand the Higgs potential. Once we choose a minimum,

we can write an effective scalar potential $V(H)$ that represents deviations about this minimum. The first terms of the new Higgs potential can be written as:

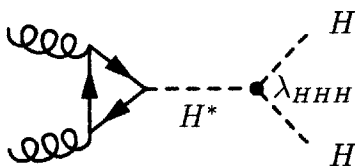
$$V(H) = \frac{1}{2}M_H^2 H^2 + \frac{1}{6}\lambda_{HHH}H^3 + \dots \quad (2.2)$$

The value for λ_{HHH} is predicted by the Standard Model once M_H is known:

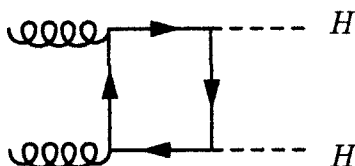
$$\lambda_{HHH} = \frac{3M_H^2}{v}, \quad (2.3)$$

Here, v is the vacuum expectation value coming from the shape of the Higgs potential and known to be 246 GeV from the masses of the W^\pm and Z bosons in the Standard Model.

The self-coupling constant λ_{HHH} in front of the cubic term in the expanded Higgs potential determines the strength of self-interactions where three Higgs bosons appear at a single vertex. Such a vertex would occur in Feynman diagrams for events where an off-shell Higgs decays into two on-shell Higgs bosons. This paper focuses is on di-Higgs production via gluon fusion.



The same initial and final states can also appear in events without Higgs self-coupling, albeit with a smaller cross-section.



Both diagrams include quark loops (primarily top quarks) in their Higgs production. Because the two diagrams show the same initial and final states, the processes they represent interfere with one another. As a result, any program that simulates di-Higgs production via gluon fusion $gg \rightarrow HH$ must include both processes.

One way to test the consistency of λ_{HHH} with the value predicted by the Standard Model is to measure the frequency of di-Higgs production. Studies conducted by Refs. [1] and [2] have looked into the effects of varying the coupling constant on the number of observed di-Higgs events. Figure 2.2 shows how the expected cross-section varies as λ_{HHH} changes relative to λ_{HHH}^{SM} .

The vertical axis of Figure 2.2 gives the ratio of $\sigma(pp \rightarrow HH + X)$ to σ^{SM} : the cross section for producing two Higgs during proton-proton collisions divided by the Standard Model cross section. The horizontal axis gives the ratio of the coupling

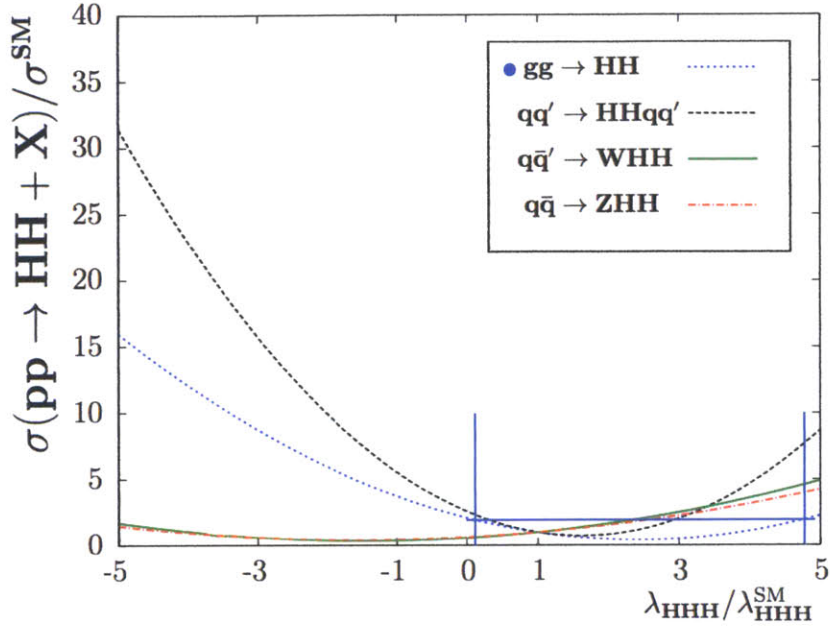


Figure 2.2: Plot adapted from Ref. [1] of the fractional change in the expected cross-section for di-Higgs production when λ_{HHH} is varied from its Standard Model value λ_{HHH}^{SM} .

constant λ_{HHH} to the Standard Model coupling constant λ_{HHH}^{SM} . When this ratio $\lambda_{HHH}/\lambda_{HHH}^{SM}$ is 1, $\sigma(pp \rightarrow HH + X)/\sigma^{SM}$ is also 1, since this is the case where the Standard Model is correct in its prediction for λ_{HHH} . As the coupling constant λ_{HHH} changes, however, the expected cross-section also changes, hence the parabolic shaped curves.

The four different curves plotted correspond to different channels for producing two Higgs bosons. In the plot in Figure 2.2, the $gg \rightarrow HH$ channel is not the highest curve because other channels can exhibit a larger percent change in $\sigma(pp \rightarrow HH + X)$ as λ_{HHH} is varied. This study focuses on the $gg \rightarrow HH$ channel, however, because that channel has the largest overall cross-section, making it the most common and most promising production method to analyze.

The solid blue lines overlaid on Figure 2.2 illustrate how to interpret the plot to place limits on the ratio $\lambda_{HHH}/\lambda_{HHH}^{SM}$. The horizontal line is placed at $\sigma(pp \rightarrow HH + X)/\sigma^{SM} = 2$. The vertical lines appear where this horizontal line intersects the dashed blue curve corresponding to the $gg \rightarrow HH$ channel. If one can determine that the number of signal events observed is consistent with a production cross section of less than 2 times the Standard Model cross-section, then the plot from Ref. [1] restricts the ratio $\lambda_{HHH}/\lambda_{HHH}^{SM}$ to the region between the vertical lines starting just above 0 and ending just below 5. Narrowing the size of the possible range for λ_{HHH}

thus requires an ability to exclude cross-sections for $gg \rightarrow HH$ a fraction larger than predicted by the Standard Model.

Since the probabilities for different Higgs decays are known (called branching ratios), one can draw conclusions about the total cross-section for $gg \rightarrow HH$ by finding the cross-section for the particular decay mode $gg \rightarrow HH \rightarrow b\bar{b}\tau\bar{\tau}$. This $b\bar{b}\tau\bar{\tau}$ channel has been predicted to be one of the most promising for characterizing λ_{HHH} at CMS [1].

Chapter 3

Simulating Di-Higgs Production

3.1 Cross-sections for Self-Coupling

For the measured Higgs mass $M_H = 125$ GeV, the total SM cross-section for $gg \rightarrow HH$ in proton-proton collisions is 8.2 fb at $\sqrt{s} = 8$ TeV. At $\sqrt{s} = 14$ TeV, the cross-section is 33.9 fb; and at $\sqrt{s} = 100$ TeV, it is 1418 fb. The CMS experiment currently has 21.8 fb^{-1} of data recorded at $\sqrt{s} = 8$ TeV in 2012 and another 5.6 fb^{-1} of data at $\sqrt{s} = 7$ TeV from 2011. The LHC is in the process of being upgraded to allow it to obtain center of mass energies of 13 TeV. CMS plans to restart collecting data in 2015. The current design limit of the LHC is 14 TeV and future upgrades to 20 TeV are foreseeable. An upgrade to 100 TeV is not possible, however, and would require a new accelerator.

Since the total number of expected events in a data set is proportional to both the cross-section and the integrated luminosity, the number of di-Higgs events in a sample can increase by: 1) running the LHC longer at a lower energy to increase the integration time; 2) decreasing the bunch spacing to make collisions more frequent and thus increase the detector's instantaneous luminosity; or 3) increasing the energy of the collisions to increase the production cross-section. There are plans to increase the instantaneous luminosity of the LHC in the coming decades.

3.2 Simulation Tools

Because the cross-section for $gg \rightarrow HH$ is so low at 8 TeV, CMS does not expect to find many events in its current data set. In order to make predictions for future analyses at a higher integrated luminosity, this study uses Madgraph to simulate di-Higgs production events. Madgraph is a program that simulates leading-order processes for user-specified interactions by performing quantum field theory computations numerically. These interactions can be more complicated than the decays simulated by Pythia (a program commonly used for simulation studies). Madgraph

takes the parton distribution function of gluons and quarks for two colliding protons and generates four-vectors for the initial gluons and final-state Higgs bosons in the $gg \rightarrow HH$ process. The initial gluons were set to have three-momenta aligned with the beam axis. Both Feynman diagrams in Chapter 2 were included as possible interactions and weighted based on their relative cross-sections. The result was an LHE file that lists the four-vectors for the initial and final state particles in each event in a plain text format. Pythia can then be used to load the LHE file and simulate decays of the two Higgs bosons, while GEANT simulates interactions with the detector.

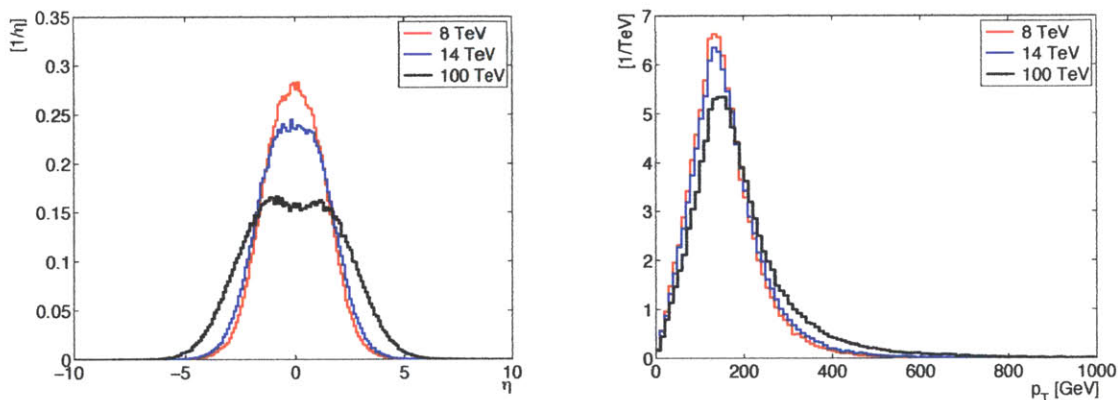


Figure 3.1: Combined η and p_T distributions for the two Higgs bosons generated by Madgraph at center of mass energies of 8, 14, and 100 TeV.

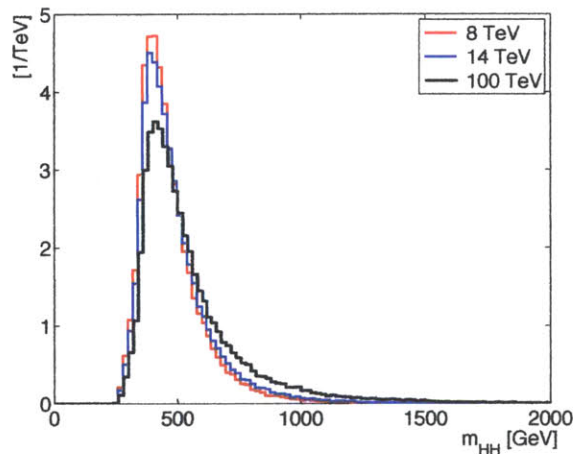


Figure 3.2: Di-Higgs center of mass energy, corresponding to the mass distribution for the off-shell Higgs boson in decays involving Higgs self-coupling.

In this study 100,000 $gg \rightarrow HH$ events were simulated for each of three center of mass energies: $\sqrt{s} = 8, 14,$ and 100 TeV. Kinematical plots are shown in Figures 3.1 and 3.2. These plots were compared to the results of Ref. [1] as a cross-check of the event generation methods. Figures 3.1 and 3.2 show how the η , p_T , and m_{HH} distributions for the two Higgs bosons produced vary with energy. The η and p_T plots are probability distributions that include both of the Higgs bosons produced. The m_{HH} probability distribution was arrived at by summing the four-vectors for the two individual Higgs bosons to determine the mass of the single off-shell Higgs boson they would have decayed from if the event corresponded to the first Feynman diagram in Chapter 2. In Madgraph, both Feynman diagrams are included to take into account the interference between the two processes. Since the 8 TeV and 14 TeV simulations are relevant to both the current data set and the anticipated 2015 data set, the four-vectors from the two resultant Higgs bosons in the 8 TeV and 14 TeV LHE files were then imported into Pythia and GEANT to simulate their decay and perform a detector acceptance study.

Chapter 4

Decay Channels

4.1 Restriction to $HH \rightarrow b\bar{b}\tau\bar{\tau}$

This study examines the $HH \rightarrow b\bar{b}\tau\bar{\tau}$ channel because that channel is more common than most Higgs decay modes. Although $H \rightarrow b\bar{b}$ is the most common single Higgs decay, making $HH \rightarrow b\bar{b}b\bar{b}$ the most likely di-Higgs decay, $HH \rightarrow b\bar{b}b\bar{b}$ events are similar to a larger number of background processes. The larger relative background compared to signal reduces the $HH \rightarrow b\bar{b}b\bar{b}$ channel's utility for studying λ_{HHH} . The branching ratio for $H \rightarrow b\bar{b}$ is 57.7%, while the branching ratio for $H \rightarrow \tau\bar{\tau}$ is only 6.3%. The $gg \rightarrow HH$ cross-section for each energy is reduced by a factor:

$$f = 2 \times BR(H \rightarrow b\bar{b}) \times BR(H \rightarrow \tau\bar{\tau}) = 7.29 \times 10^{-2} \quad (4.1)$$

where the 2 comes from $HH \rightarrow b\bar{b}\tau\bar{\tau}$ and $HH \rightarrow \tau\bar{\tau}b\bar{b}$ being equivalent. The expected cross-section for $gg \rightarrow HH \rightarrow b\bar{b}\tau\bar{\tau}$ is thus the cross-section for $gg \rightarrow HH$ set forth in Chapter 3 multiplied by f .

In Pythia, the two Higgs bosons were restricted to decay into $HH \rightarrow b\bar{b}\tau\bar{\tau}$. Splitting the di-Higgs events generated by Madgraph and having one Higgs from each event decay $H \rightarrow b\bar{b}$ and the other $H \rightarrow \tau\bar{\tau}$, provided more statistics for the $HH \rightarrow b\bar{b}\tau\bar{\tau}$ events for a fixed number of generated events. This method for decaying the two Higgs bosons independently is more efficient than the standard procedure of taking all of the $gg \rightarrow HH$ events and allowing the two Higgs to decay into either $\tau\bar{\tau}$ or $b\bar{b}$. In the standard procedure, the majority of events would be $HH \rightarrow b\bar{b}b\bar{b}$ because the branching ratio for $H \rightarrow b\bar{b}$ is an order of magnitude larger than that for $H \rightarrow \tau\bar{\tau}$. In this study, the cross-section for the generated events is equal to the $gg \rightarrow HH \rightarrow b\bar{b}\tau\bar{\tau}$ cross-section.

4.2 Detected Final States

The b quarks and τ 's are not detected directly, however. Instead, CMS detects their decay products. Events are identified as having produced a $b\bar{b}$ pair when they contain two jets that pass a b -tagging selection. The two τ 's decay too quickly to interact with the detector. They undergo either hadronic or leptonic decays. These processes start with:

$$\tau^- \rightarrow \nu_\tau + W^- . \quad (4.2)$$

In general, a τ^\pm decays through the weak interaction into a W^\pm boson. This W^\pm can then decay into either two quarks or a lepton with a longer decay time. For instance:

$$W^- \rightarrow \bar{u} + d, \quad W^- \rightarrow \bar{\nu}_\mu + \mu^- \quad (4.3)$$

are two possible decays. A hadronic decay is detected as pions reconstructed as a τ_{had} , while a leptonic decay produces either an e or a μ , which is detected in a separate region of the CMS detector (either the electromagnetic calorimeter or the muon chambers of Figure 1.1). In addition, each τ decay produces 1 or 2 neutrinos that go undetected except as a missing transverse energy. The energy deficit can be used to apply corrections when reconstructing the mass of the initial decay product. The final states of interest in this study are $b\bar{b}\tau_{\text{had}}\tau_{\text{had}}$, $b\bar{b}\mu\tau_{\text{had}}$, $b\bar{b}e\tau_{\text{had}}$, $b\bar{b}e\mu$, where the inclusion of a τ_{had} , when referencing the final state, indicates a hadronic τ decay. The branching ratio for $\tau \rightarrow \nu_\tau \bar{\nu}_e e^-$ is 17.8%, while $\tau \rightarrow \nu_\tau \bar{\nu}_\mu \mu^-$ is 17.4% cf. Ref. [3]. Thus, the final states that include hadronic decays will occur more frequently.

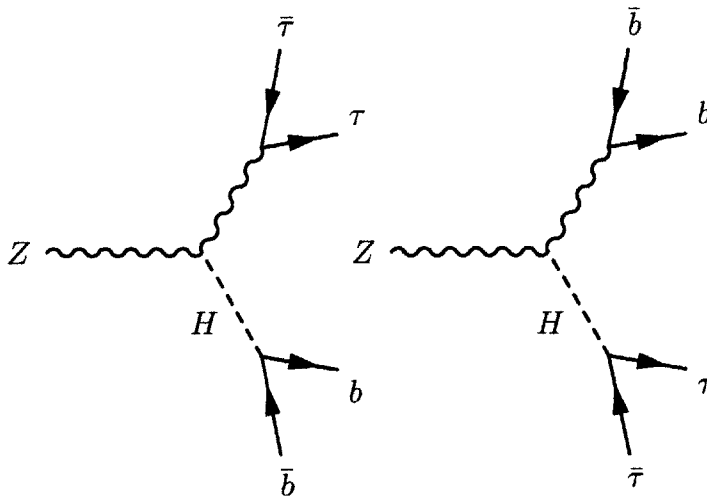
Chapter 5

Background Processes

The source of $b\bar{b}\tau\bar{\tau}$ final states could also be background processes, such as ZH and $t\bar{t}$. These are the two primary backgrounds when selecting $HH \rightarrow b\bar{b}\tau\bar{\tau}$ events. This study considered ZH and $t\bar{t}$ backgrounds to estimate if the signal to background ratio will be sufficient for CMS to draw conclusions about λ_{HHH} .

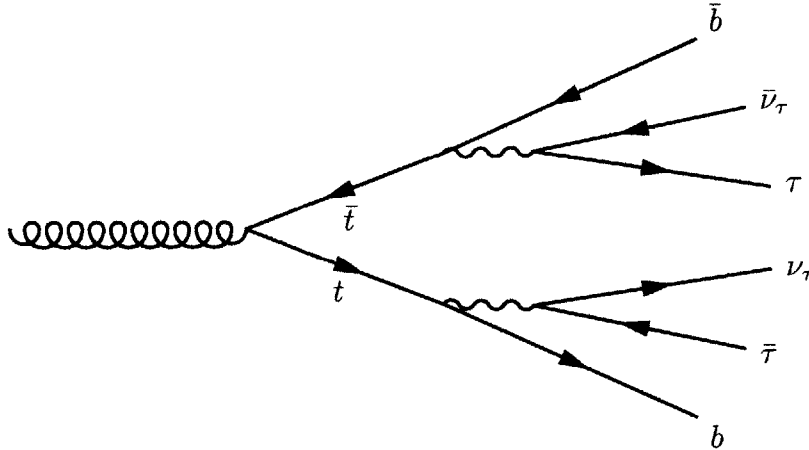
5.1 ZH Background

In Higgs-strahlung VH events, an off-shell vector boson ($V = Z$ or W^\pm) radiates a Higgs boson. For ZH , a Z boson emits a Higgs boson and then can decay $Z \rightarrow b\bar{b}$ or $Z \rightarrow \tau\bar{\tau}$, while the Higgs can decay $H \rightarrow \tau\bar{\tau}$ or $H \rightarrow b\bar{b}$. In both cases, the decay to $b\bar{b}$ is favored. Events with one $b\bar{b}$ and one $\tau\bar{\tau}$ decay would pass the same b -jet and τ selections; but only one of the decay pairs should have a reconstructed mass close to $M_H = 125$ GeV since the second pair comes from a Z decay, where $M_Z = 91$ GeV. The ZH decays correspond to the following two Feynman diagrams:



5.2 $t\bar{t}$ Background

The second background considered in this study is $t\bar{t} \rightarrow b\bar{b}\tau\bar{\tau}\nu_\tau\bar{\nu}_\tau$. In this process, a $t\bar{t}$ pair decays via the weak interaction into two b quarks and two W bosons. These W bosons can then decay into τ and τ -neutrino pairs. Although $b\bar{b}\tau\bar{\tau}$ are included in the final state, the two b -jets and two τ 's do not originate as pairs that decayed from the same initial particle. The reconstructed masses of the b -jet and τ pairs therefore should not correlate strongly. By contrast, the signal and ZH background would have peaks in $M_{b\bar{b}}$ and $M_{\tau\bar{\tau}}$ corresponding to M_H and M_Z .



Although only the $t\bar{t} \rightarrow b\bar{b}\tau\bar{\tau}\nu_\tau\bar{\nu}_\tau$ decay mode for $t\bar{t}$ has the same final states as $gg \rightarrow HH \rightarrow b\bar{b}\tau\bar{\tau}$, the subsequent decays of the τ 's make it important to consider other $t\bar{t}$ decays. When the W bosons decay into leptons of other flavors, the same detected final states result as when the τ from a $HH \rightarrow b\bar{b}\tau\bar{\tau}$ decay subsequently undergoes a leptonic decay into an e or μ . As such, $t\bar{t}$ is a significant source of background events.

5.3 Background Simulation

Two VH and $t\bar{t}$ Monte Carlo (MC) samples were passed through the same selection cuts applied to the simulated signal events. These background data sets had been generated for $\sqrt{s} = 8$ TeV and at $M_H = 125$ GeV for the VH events. The cross-section for the $t\bar{t}$ events is 225 pb at $\sqrt{s} = 8$ TeV and will be 877 pb at $\sqrt{s} = 14$ TeV [4]. Although ZH is the background of interest, other VH events were part of a second background sample generated for current CMS $\tau\tau$ analyses. Those VH events include:

1. ZH ($\sigma_{8TeV} = 0.394$ pb, $\sigma_{14TeV} = 0.883$ pb)
2. WH ($\sigma_{8TeV} = 0.697$ pb, $\sigma_{14TeV} = 1.504$ pb)
3. ttH ($\sigma_{8TeV} = 0.130$ pb, $\sigma_{14TeV} = 0.611$ pb)

components. WH events have a W^\pm boson in place of the Z boson, while ttH events include a Higgs boson produced in association with a $t\bar{t}$ pair. Chapter 6 describes selection cuts that will eliminate these second and third backgrounds when $b\bar{b}\tau\bar{\tau}$ final states are chosen. It is important to recognize that all three types of events are part of the background sample, however, since they affect the normalization that should be used to compute the effective cross-section (Section 6.1) for selecting background events by looking at the fraction that pass selection cuts.

This study also restricted the MC generation for the VH events to $H \rightarrow \tau\bar{\tau}$ decays, giving a total cross-section of 77.2 fb for $\sqrt{s} = 8$ TeV and 189.5 fb for $\sqrt{s} = 14$ TeV. Because of this restriction on Higgs decays, the background events that pass the selection cuts will correspond to the right-hand ZH Feynman diagram above, where the H decays into a $\tau\bar{\tau}$ pair.

To accumulate enough statistics to generate histograms of kinematical variables for the signal and background MC events that pass the signal selections, $\sim 200\text{k}$ VH and $\sim 6\text{M}$ $t\bar{t}$ events were included in the samples sent through the $b\bar{b}\tau\bar{\tau}$ selection process.

Chapter 6

Event Selection

6.1 Effective Cross-Section

All of the generated signal events were $HH \rightarrow b\bar{b}\tau\bar{\tau}$. Therefore, the fraction making it through selection cuts estimates the expected detector acceptance. The restriction to $b\bar{b}\tau_{\text{had}}\tau_{\text{had}}$, $b\bar{b}\mu\tau_{\text{had}}$, $b\bar{b}e\tau_{\text{had}}$, $b\bar{b}e\mu$ reduces the total number of applicable events, even for an ideal reconstruction and acceptance.

Selection cuts were performed on the reconstructed MC events to determine what fraction of $HH \rightarrow b\bar{b}\tau\bar{\tau}$ made it through the reconstruction, isolation cuts, and kinematic cuts on each τ decay product and jet. This resulted in an effective cross section for detecting these events at CMS equal to the fraction of events that pass the selection times the $gg \rightarrow HH \rightarrow b\bar{b}\tau\bar{\tau}$ cross section:

$$\sigma_{eff} = \frac{\# \text{ passing events}}{\# \text{ MC events}} \times f\sigma_E, \quad (6.1)$$

where f is the factor from Eq. (4.1) and σ_E is the \sqrt{s} -dependent $gg \rightarrow HH$ cross-section. The number of detected events expected in an actual data set after accumulating an integrated luminosity $\int \mathcal{L}dt$ is then:

$$N = \int \mathcal{L}dt \times \sigma_{eff}. \quad (6.2)$$

Computing σ_{eff} thus provides a basis to evaluate how well CMS will be able to characterize Higgs self-coupling through the $gg \rightarrow HH \rightarrow b\bar{b}\tau\bar{\tau}$ channel, by estimating how much data at a given \sqrt{s} will be needed to accumulate a specified number of events.

6.2 Final State Identification

The MC events were passed through selections that identified those matching one of the four final states. These four ntuples for each original $gg \rightarrow HH$ generation were

then passed through isolation cuts depending upon the type of τ decay. The isolation variable for leptonic decays characterizes the signal to background separation in a $\Delta R = \sqrt{\Delta\phi^2 + \Delta\eta^2}$ cone around the lepton. The smaller this parameter, the better isolated the lepton candidate. For hadronic decays, the isolation variable corresponds to a measure of how signal-like the τ candidate is. A larger value means it is more likely a τ_{had} .

After applying isolation cuts, the leading and next-to-leading jets (based on p_T) went through a medium cut on a combined secondary vertex variable (jcsv) to identify them as b -jet candidates. This single discriminant takes into account multiple kinematical properties characteristic of b -jets and requires resolving a secondary decay vertex. Since hadrons containing b quarks can have a time of flight ~ 1.5 ps, the displacement between locations where the b quark is produced and where it decays can be resolved. The efficiency of b -tagging is on the order of $\sim 50\%$ [5]. This b -tagging efficiency reduces the number of MC b -jet events that will actually be identified as such.

Limiting the two leading jets to b -jets further reduces the chance that the $\sim 100,000$ generated $gg \rightarrow HH \rightarrow b\bar{b}\tau\bar{\tau}$ will pass a $b\bar{b}$ selection cut, since other jets with different flavors can also be produced in the decay of $gg \rightarrow HH$ simulated by Pythia. Events with more than two jets could contain two b -tagged jets that do not have the largest and second largest p_T .

6.3 Kinematical Cuts

In addition to requiring that the reconstructed events have two τ 's and two b -jets, kinematic cuts were applied to compare selection efficiencies with those predicted by Ref. [1]:

1. $p_T > 30$ GeV
2. $|\eta| < 2.4$
3. $112.5 \text{ GeV} < M_{b\bar{b}} < 137.5 \text{ GeV}$
4. $100 \text{ GeV} < M_{\tau\bar{\tau}} < 150 \text{ GeV}$

where $M_{b\bar{b}}$ and $M_{\tau\bar{\tau}}$ are the reconstructed center of mass energies of the two b -jets, and τ 's, respectively. In the case of a decay from a single particle, the center of mass energy equals the mass of that parent particle. The di-lepton mass includes corrections to compensate for the undetected neutrinos produced.

The first two cuts restrict passing events to those with high enough p_T and small enough pseudo-rapidity η for all four final state $b\bar{b}\tau\bar{\tau}$ candidates to hit regions of the detector that can identify more reliably b -jets and τ 's. Constraining the di-jet and di- τ reconstructed masses to an interval surrounding the Higgs mass decreases the number of background events that would pass these signal selection cuts.

6.4 Signal vs. Background

While each selection cut will reduce the number of signal events that pass, the goal is to choose selections that optimize the signal to background ratio. A larger signal to background ratio strengthens the analysis. The relative signal versus background dictates how well CMS can characterize λ_{HHH} .

Consider an example that illustrates how a large cross-section can be excluded when only a few events are observed. In the limit of large statistics, the probability of observing a certain number of events would follow a Poisson distribution with mean $S + B$ since the number of events that are expected to pass selection cuts will be S signal events and B background events if the Standard Model is correct. In the limit where $S + B$ is large, the uncertainty on the total number of signal and background events observed would be $\sqrt{S + B}$.

Now, consider the further limit where the number of signal events S is small compared to the number of background events B , while B is large enough for the Poisson uncertainty to still be $\sqrt{S + B} \approx \sqrt{B}$. Excluding $\sigma/\sigma_{SM} > 2$ would be equivalent to saying that $2S + B$ is ≥ 2 standard deviations away from $S + B$ (i.e. observing twice the signal plus the same background would be expected to occur around 2% of the time). This would mean $S \geq 2\sqrt{B}$.

Following the same procedure, excluding $\sigma/\sigma_{SM} > N$ for $N > 1$ would require that $S \geq \frac{2}{N-1}\sqrt{B}$ or, equivalently, $S/\sqrt{B} \geq \frac{2}{N-1}$. This rough estimate shows how restricting σ/σ_{SM} , and thus $\lambda_{HHH}/\lambda_{HHH}^{SM}$, to a smaller range becomes more difficult. It also illustrates how S/\sqrt{B} can be used as a metric for evaluating how well a process can be detected. Since both S and B scale with $\int \mathcal{L} dt$, S/\sqrt{B} scales as $\sqrt{\int \mathcal{L} dt}$. For cases where S and B are both small, the Poisson nature of the $S + B$ and B distributions must be treated without making Gaussian-limit approximations, cf. Ref. [6].

Chapter 7

Results

7.1 Effective Cross-Section Values

The signal and background MC events were first sent through four coarse selections for the $\tau_{\text{had}}\tau_{\text{had}}$, $\mu\tau_{\text{had}}$, $e\tau_{\text{had}}$, $e\mu$ final states for the two τ 's. To compare this study to the results of Ref. [1], two rounds of cuts were applied: first, a selection for two τ 's meeting the requirements in Chapter 6; second, a selection for two b -jets. The results of these selections are summarized in Tables 7.1 and 7.2 for $\sqrt{s} = 8$ TeV and $\sqrt{s} = 14$ TeV. The first row gives the production cross-section for the MC events included in the study described in Chapter 5. The second and third sets of rows are computed by finding the fraction of generated events that make it through the selections and multiplying that fraction by the cross-section σ_{SM} for the initial process the events came from. The total is also broken down by τ decay mode. For the first round of $H \rightarrow \tau\bar{\tau}$ cuts, a few hundred events passed each cut, reducing uncertainties on the effective cross-section to 5% or less. After the $H \rightarrow b\bar{b}$ cut, only a handful of MC events passed from the VH sample, increasing the fractional uncertainty. However, the dominant source of background when computing S/B was $t\bar{t}$.

Using the $gg \rightarrow HH$ cross-sections of 8.2 fb at $\sqrt{s} = 8$ TeV and 33.9 fb at $\sqrt{s} = 14$ TeV, the computations in Chapter 4 show that the expected cross-sections for $gg \rightarrow HH \rightarrow b\bar{b}\tau\bar{\tau}$ are $\sigma_{SM} = 0.6$ fb at $\sqrt{s} = 8$ TeV and $\sigma_{SM} = 2.5$ fb at $\sqrt{s} = 14$ TeV. These cross-sections appear as the starting point for the computation of σ_{eff} . The requirement of detecting two τ 's and two b -jets reduces this cross-section by two orders of magnitude.

7.2 Comparison to Prediction

The result for the 14 TeV MC signal data, the HH column of Table 7.2, can be compared directly to the HH column of Table 7.3, which shows the effective cross-sections assumed by the study in Ref. [1]. The order-of-magnitude reduction in σ_{eff}

MC 8	HH	VH	$t\bar{t}$	S/B
σ_{SM} [fb]	5.95×10^{-1}	7.72×10^1	2.25×10^5	2.64×10^{-6}
$H \rightarrow \tau\bar{\tau}$	3.34×10^{-2}	2.18	7.78×10^2	4.28×10^{-5}
$\tau_{\text{had}}\tau_{\text{had}}$	1.25×10^{-2}	7.15×10^{-1}	3.08×10^1	3.95×10^{-4}
$\mu\tau_{\text{had}}$	1.04×10^{-2}	4.45×10^{-1}	2.56×10^2	4.07×10^{-5}
$e\tau_{\text{had}}$	8.39×10^{-3}	7.60×10^{-1}	1.63×10^2	5.11×10^{-5}
$e\mu$	2.16×10^{-3}	2.64×10^{-1}	3.28×10^2	6.58×10^{-6}
$H \rightarrow b\bar{b}$	4.21×10^{-3}	3.09×10^{-3}	1.56×10^1	2.69×10^{-4}
$\tau_{\text{had}}\tau_{\text{had}}$	1.54×10^{-3}	7.72×10^{-4}	6.97×10^{-1}	2.21×10^{-3}
$\mu\tau_{\text{had}}$	1.35×10^{-3}	3.86×10^{-4}	4.68	2.88×10^{-4}
$e\tau_{\text{had}}$	1.01×10^{-3}	1.54×10^{-3}	2.33	4.36×10^{-4}
$e\mu$	3.01×10^{-4}	3.86×10^{-4}	7.94	3.79×10^{-5}

Table 7.1: Effective cross-section [fb] found after selecting for $\tau\bar{\tau}$ and $b\bar{b}$ decay products for MC signal and background events, shown for $\sqrt{s} = 8$ TeV.

MC 14	HH	VH	$t\bar{t}$	S/B
σ_{SM} [fb]	2.47	1.90×10^2	8.77×10^5	2.82×10^{-6}
$H \rightarrow \tau\bar{\tau}$	1.18×10^{-1}	5.37	3.03×10^3	3.88×10^{-5}
$\tau_{\text{had}}\tau_{\text{had}}$	3.82×10^{-2}	1.76	1.20×10^2	3.14×10^{-4}
$\mu\tau_{\text{had}}$	3.97×10^{-2}	1.09	9.96×10^2	3.98×10^{-5}
$e\tau_{\text{had}}$	3.04×10^{-2}	1.87	6.37×10^2	4.76×10^{-5}
$e\mu$	9.53×10^{-3}	6.48×10^{-1}	1.28×10^3	7.44×10^{-6}
$H \rightarrow b\bar{b}$	1.57×10^{-2}	7.60×10^{-3}	6.10×10^1	2.58×10^{-4}
$\tau_{\text{had}}\tau_{\text{had}}$	5.15×10^{-3}	1.90×10^{-3}	2.72	1.89×10^{-3}
$\mu\tau_{\text{had}}$	5.40×10^{-3}	9.49×10^{-4}	1.83×10^1	2.96×10^{-4}
$e\tau_{\text{had}}$	3.95×10^{-3}	3.80×10^{-3}	9.06	4.35×10^{-4}
$e\mu$	1.23×10^{-3}	9.49×10^{-4}	3.09×10^1	3.98×10^{-5}

Table 7.2: Effective cross-section [fb] found after selecting for $\tau\bar{\tau}$ and $b\bar{b}$ decay products for MC signal and background events, shown for $\sqrt{s} = 14$ TeV.

Ref. [1]	HH	ZH	$b\bar{b}\tau\bar{\tau}\nu_\tau\bar{\nu}_\tau$	S/B
σ_{SM} [fb]	2.47	2.46×10^1	8.17×10^3	3.01×10^{-4}
$H \rightarrow \tau\bar{\tau}$	2.09×10^{-1}	5.70×10^{-1}	1.58×10^2	1.32×10^{-3}
$H \rightarrow b\bar{b}$	1.46×10^{-1}	3.75×10^{-2}	1.43×10^1	1.02×10^{-2}

Table 7.3: Effective cross-section from Ref. [1] after selecting for $\tau\bar{\tau}$ and $b\bar{b}$ decay products, shown for $\sqrt{s} = 14$ TeV.

shows that the b -tagging and τ reconstruction algorithms are less efficient than the 70% b -tagging efficiency and 50% τ -tagging quoted. Table 7.4 illustrates the breakdown between the effects of these two cuts. Here, results for 14 TeV are given as the expected fraction of events passing each successive round of cuts: 1) $\tau\bar{\tau}$ selection, 2) $b\bar{b}$ selection. The HH column provides a direct measure of the expected selection efficiencies for τ and b -tagging.

The τ -tagging efficiency is nearly a factor of two smaller than predicted by Ref. [1]. The initial reduction after τ selection stems from three sources. First, only one quarter make it through as $\tau\bar{\tau}$ candidates in the pre-selection for four $\tau\bar{\tau}$ final states. From these, around 40% pass isolation cuts. Finally, just under half of these pass the kinematic cuts on the τ 's outlined in Chapter 6.

MC 14	HH	VH	$t\bar{t}$	Ref. [1]	HH	ZH	$b\bar{b}\tau\bar{\tau}\nu_\tau\bar{\nu}_\tau$
cut 1	0.048	0.028	0.003	cut 1	0.085	0.023	0.019
cut 2	0.134	0.001	0.020	cut 2	0.698	0.066	0.090

Table 7.4: Fraction of events that pass each round of selection cuts, shown for the 14 TeV MC data on the left and for the simulation in Ref. [1] on the right.

Fewer events pass the b -tagging and kinematical requirements than predicted by Ref. [1]. This screening results because just over 20% of the $\tau\bar{\tau}$ events pass the b -tagging requirement on the two leading jets and, then, only around 60% of those pass the cuts on kinematical variables. Although Ref. [1] claims the assumed b -tagging efficiency to be 70%, because $0.7 \times 0.7 = 0.49 \rightarrow 49\%$ passing, a 70% pass rate in Table 7.4 between the $\tau\bar{\tau}$ and $b\bar{b}$ cuts suggest either a correlation between one b -jet passing and the second one passing, or some correlation between passing the $\tau\bar{\tau}$ selection and passing the b -tagging requirements. Only a $\sim 1\%$ improvement resulted from looking at events that passed the $\tau\bar{\tau}$ isolation and kinematic cuts, compared to those that passed just the τ isolation cuts. Without assuming any correlations, an effective b -tagging efficiency of around 50% would be consistent with the results of this study.

The differences between the values in the first and second set of rows for the VH/ZH and $t\bar{t}/b\bar{b}\tau\bar{\tau}\nu_\tau\bar{\nu}_\tau$ columns in Tables 7.2 and 7.3 stem from the different background samples used. The Monte Carlo samples in this study contained VH decays restricted to $H \rightarrow \tau\bar{\tau}$. Although the $\tau\bar{\tau}$ and $b\bar{b}$ selections reduce this sample to ZH events, a sample containing only ZH events and a $b\bar{b}\tau\bar{\tau}$ final state could contain both of the ZH diagrams shown in Chapter 5.

This study utilized a larger, less restricted, sample of $t\bar{t}$ background events. Whereas the Ref. [1] considers a $b\bar{b}\tau\bar{\tau}\nu_\tau\bar{\nu}_\tau$ background, which is dominated by $t\bar{t}$ events, the MC sample in this study did not restrict the $t\bar{t}$ decays.

As a result of these differences, the σ_{eff} for ZH background is diminished, while the σ_{eff} for $t\bar{t}$ is increased compared to Ref. [1]. This result is consistent with the $H \rightarrow b\bar{b}$ and $Z \rightarrow \tau\bar{\tau}$ decay not being included in the VH background. The extra W decays to e or μ are included in this study's $t\bar{t}$ sample, but not in Ref. [1]. Because $t\bar{t}$ decays are the dominant source of background, this increase in $t\bar{t}$ background decreases the expected signal to background ratio, given in the last column of Table 7.2.

7.3 Evaluating Backgrounds

The fact that the background samples used in this study were generated at 8 TeV and not 14 TeV should also be considered. Although the cross-sections were scaled to their appropriate values, the cuts on kinematical variables could be affected. Higher p_T might be expected at 14 TeV. Higher p_T would tend to increase the number of events with τ 's and b -jets passing a 30 GeV p_T threshold. At the same time, collisions are also likely to have a larger net momentum along the beam axis, increasing the pseudo-rapidity η , and thus decreasing the likely-hood of falling into the $|\eta| < 2.4$ barrel region of the CMS detector.

The 8 TeV and 14 TeV signal Monte Carlo samples can be compared, however. Figures 7.1 and 7.2 show the reconstructed di-lepton and di-jet masses. The di-lepton mass is corrected to take into account the energy lost to neutrinos. The neutrinos prevent simply identifying the detected $\tau\bar{\tau}$ decay products and summing their four-vectors to find the mass of the parent particle. Although $M_{\tau\bar{\tau}}$ should be 125 GeV for an $H \rightarrow \tau\bar{\tau}$ decay, Figure 7.1 shows a peak at a slightly smaller mass in the signal histogram due to the incomplete reconstruction.

The histograms in Figures 7.1 and 7.2 have been renormalized as probability densities. The range of values for $M_{\tau\bar{\tau}}$ and $M_{b\bar{b}}$ were determined by the cuts described in Chapter 6. The top subplot in each compares the shapes of the 8 TeV and 14 TeV distributions, showing that the increase in energy to 14 TeV does not introduce significant features into the distributions for these two variables. While this comparison does not take into account a change in the number of events that will pass due to larger p_T or boosting in η , it does show that the shape of the distributions for these kinematical variables may not change significantly. For example, while the signal to background ratio may fluctuate, the locations of cuts on $M_{\tau\bar{\tau}}$ and $M_{b\bar{b}}$ to optimize this

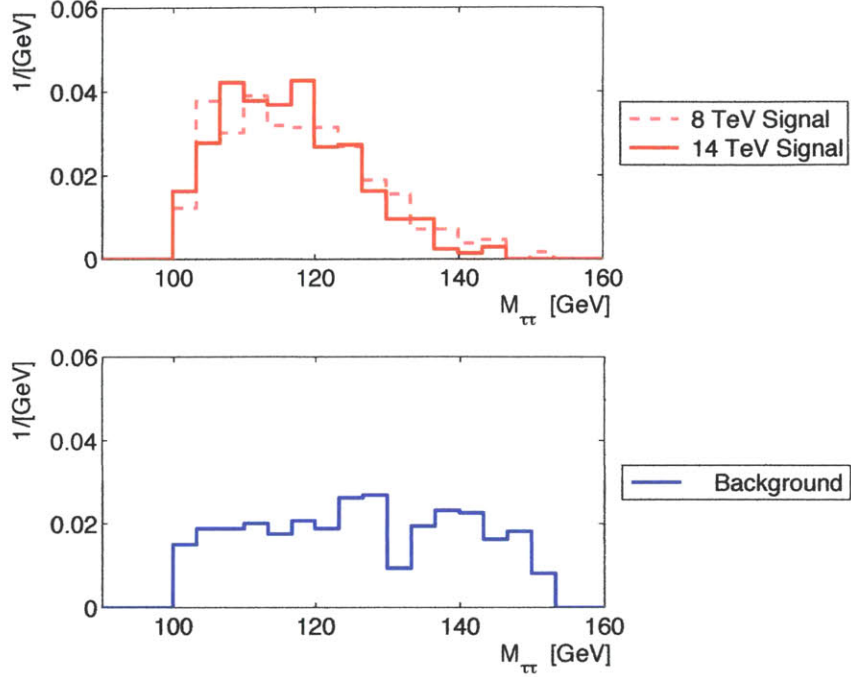


Figure 7.1: $M_{\tau\bar{\tau}}$ distribution for events passing selection cuts.

ratio should remain the same when the energy of the colliding protons is increased. Also, because branching ratios are not affected by \sqrt{s} , looking at the different $\tau\bar{\tau}$ final states can indicate ways to improve the selection cuts without excessive sensitivity to changes in the total number of background events that pass.

7.4 Comparing Final States

Figures 7.3 and 7.4 show the $M_{\tau\bar{\tau}}$ and $M_{b\bar{b}}$ distributions for the background and the 14 TeV signal in Figures 7.1 and 7.2, now broken down into components from the four $\tau\bar{\tau}$ final states: $\tau_{\text{had}}\tau_{\text{had}}$, $\mu\tau_{\text{had}}$, $e\tau_{\text{had}}$, $e\mu$. These plots reveal that while the $e\mu$ signal is the smallest contributor to the signal, it is the largest component of the background. Conversely, while the $\tau_{\text{had}}\tau_{\text{had}}$ double hadronic decay final state is a large component in the signal, it is a very small component of the total background. This contrast suggests that either restricting selected events to only some of the τ decay channels or splitting the analysis by final state can improve the signal to background ratio.

The result of applying the cuts to only the $\tau_{\text{had}}\tau_{\text{had}}$ double hadronic decay channel can be found in the $\tau_{\text{had}}\tau_{\text{had}}$ rows of Table 7.2. The result of applying the same selection cuts to all but the $e\mu$ decay channel is shown in Table 7.5. Excluding

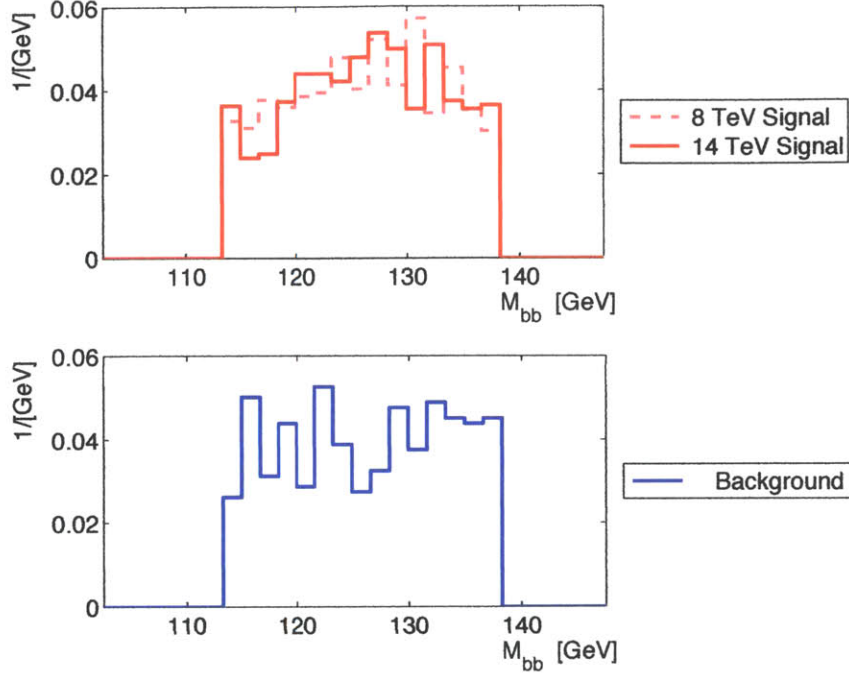


Figure 7.2: $M_{b\bar{b}}$ distribution for events passing selection cuts.

the $e\mu$ channel nearly doubles S/B without diminishing the signal σ_{eff} appreciably. Considering only the $\tau_{had}\tau_{had}$ decay channel reduces the background significantly. While S/B increases by an order of magnitude, the expected signal is cut to a third.

No $e\mu$	HH	VH	$t\bar{t}$	S/B
σ_{SM} [fb]	2.47	1.90×10^2	8.77×10^5	2.82×10^{-6}
$H \rightarrow \tau\bar{\tau}$	1.08×10^{-1}	4.72	1.75×10^3	6.16×10^{-5}
$H \rightarrow b\bar{b}$	1.45×10^{-2}	6.65×10^{-3}	3.00×10^1	4.83×10^{-4}

Table 7.5: Three channel effective cross-section [fb] found after selecting for $\tau\bar{\tau}$ and $b\bar{b}$ decay products for MC signal and background events excluding the $e\mu$ decay channel, shown for $\sqrt{s} = 14$ TeV.

Meanwhile, increasing the isolation and b -tagging requirements did not improve the signal to background ratio. This result is consistent with the nature of the background. Because the VH and $t\bar{t}$ events produce the same particles as the signal, applying stronger isolation cuts and b -tagging requirements will not reduce the background significantly. On the other hand, the small branching ratio of $\tau \rightarrow \nu_\tau \bar{\nu}_e e^-$ and $\tau \rightarrow \nu_\tau \bar{\nu}_\mu \mu^-$ from Chapter 4 shows that events that produce two τ 's will likely

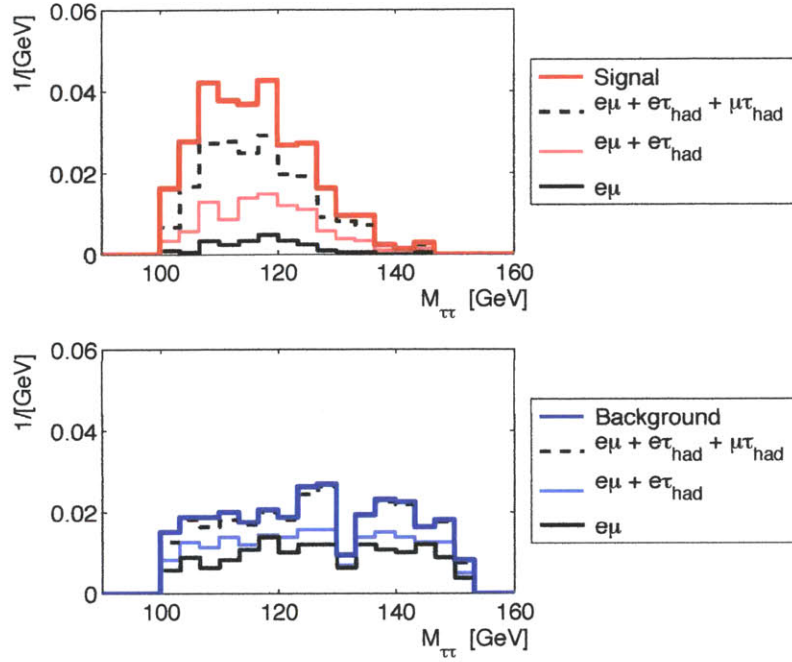


Figure 7.3: $M_{\tau\bar{\tau}}$ distribution for events passing selection cuts showing the break-down between different $\tau\bar{\tau}$ decay channels.

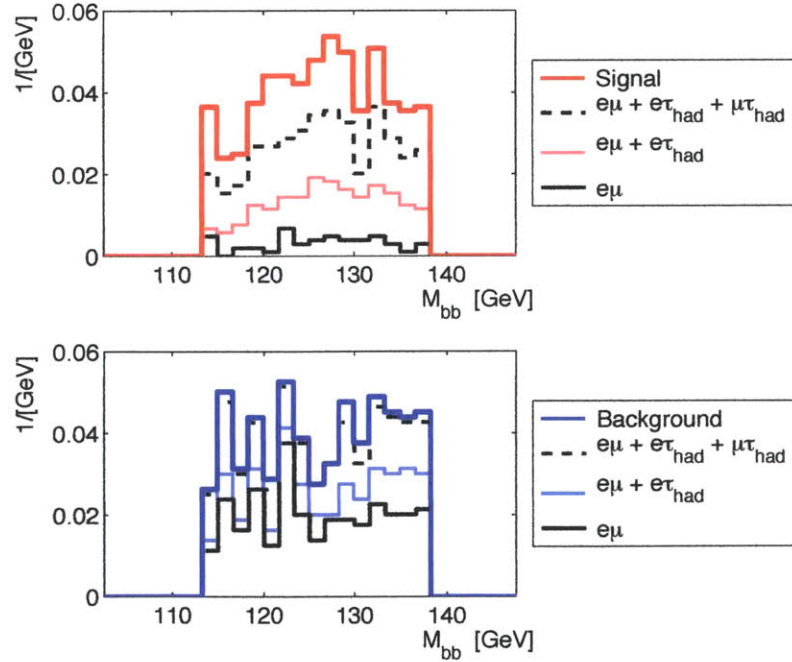


Figure 7.4: $M_{b\bar{b}}$ distribution for events passing selection cuts showing the break-down between different $\tau\bar{\tau}$ decay channels.

include hadronic, not just leptonic, decays. Removing the $e\mu$ channel or restricting selections to just the $\tau_{\text{had}}\tau_{\text{had}}$ double hadronic decay channel thus can eliminate events that produce leptons of other flavors, but no τ 's. These events exist in the background because the W bosons produced in $t \rightarrow b + W^+$ and $\bar{t} \rightarrow \bar{b} + W^-$ can decay into leptons other than τ 's. While the Higgs boson couples to mass and thus more favorably decays into $\tau\bar{\tau}$ than another lepton pair, the branching ratios for W^\pm decays to a lepton and neutrino are not as dependent on the flavor.

Chapter 8

Conclusions and Future Work

This study provides an estimate of the effective cross-section for observing Higgs self-coupling events. The number of signal and background events expected can thus be computed for a sample of data with a given integrated luminosity. Figure 2.2 then shows how to draw conclusions about the self-coupling constant from this data. For instance, $\lambda_{HHH}/\lambda_{HHH}^{SM}$ can be constrained between 0 and 5, if $\sigma/\sigma_{SM} > 2$ can be excluded.

Around 120 fb^{-1} can be expected within the first three years of resuming data collection. This rate is a function of the amount of time proton-proton collisions actually occur, and thus should improve slightly with practice. The current upgrades will increase the energy to 13 TeV. While reaching $\int \mathcal{L} dt = 300 \text{ fb}^{-1}$ is realizable within the next decade, the $\int \mathcal{L} dt = 3000 \text{ fb}^{-1}$ benchmark would not be feasible without future upgrades to the LHC beyond those already planned.

Although the theoretical literature predicts that a few hundred signal events could pass selections, this study shows that on the order of 50 would pass in the same $\int \mathcal{L} dt = 3000 \text{ fb}^{-1}$ sample size. Even fewer events would pass if restrictions on M_{HH} and $p_{T,H}$ were added. The reduced signal to background ratio also makes it harder to draw conclusions about $\lambda_{HHH}/\lambda_{HHH}^{SM}$ from these events.

This study reveals a less optimistic prediction for CMS's ability to characterize Higgs self-coupling through the $gg \rightarrow HH \rightarrow b\bar{b}\tau\bar{\tau}$ channel, compared to Refs. [1] and [2]. The order-of-magnitude reduction in signal events that pass cuts to identify $b\bar{b}\tau\bar{\tau}$ final states indicates that a study using this channel would demand larger integrated luminosities or an improvement to the efficiency of current reconstruction algorithms.

Acquiring larger $\int \mathcal{L} dt$ within a reasonable timescale would require an upgrade to the instantaneous luminosity of proton-proton collisions. Such an upgrade results in larger pileups, where multiple collisions occur during the same event. This presents a challenge the LHC will face. The CMS team is already designing work-arounds to allow more data to be collected in less time, using upgraded equipment that will not compromise their ability to distinguish all of the detectable decay products stemming from a particular collision.

While increasing the instantaneous luminosity will make a larger data set feasible, a low effective cross-section combined with a low signal-to-background ratio indicates that characterizing λ_{HHH} at CMS using $HH \rightarrow b\bar{b}\tau\bar{\tau}$ events is unlikely. During the summer of 2013, the $HH \rightarrow b\bar{b}\gamma\gamma$ channel will be studied, since its background is significantly lower. The cross-section for these $HH \rightarrow b\bar{b}\gamma\gamma$ is also much smaller, however.

At higher collision energies, near the 100 TeV mark, the di-Higgs production cross-section increases significantly. Even an upgrade to 20 TeV would push the design limits of the LHC, however. The $gg \rightarrow HH \rightarrow b\bar{b}\tau\bar{\tau}$ channel this study considered was predicted to be among the most promising channels for characterizing λ_{HHH} at CMS. A rigorous Higgs self-coupling measurement may need to wait for a new, higher energy collider that can: reach the 100 TeV mark; increase the frequency of di-Higgs events; and provide sufficient data to either restrict λ_{HHH} to a narrow range around λ_{HHH}^{SM} , validating the Standard Model Higgs potential, or demonstrate a deviation, signifying physics that extends beyond the Standard Model.

Bibliography

- [1] J. Baglio, A. Djouadi, R. Gröber, M. M. Mühlleitner, J. Quevillon and M. Spira, “The measurement of the Higgs self-coupling at the LHC: theoretical status,” arXiv:1212.5581v1 [hep-ph] (21 Dec 2012).
- [2] F. Goertz, A. Papaefstathiou, L. L. Yang and J. Zurita, “Higgs Boson self-coupling measurements using ratios of cross-sections,” arXiv:1301.3492v1 [hep-ph] (15 Jan 2013).
- [3] K. G. Hayes, “ τ Branching Fractions,” Particle Data Group (Apr 2012).
- [4] M. Cacciari, M. Czakon, M. Mangano, A. Mitov and P. Nason, “Top-pair production at hadron colliders with next-to-next-to-leading logarithmic soft-gluon resummation,” arXiv:1111.5869v2 [hep-ph] (7 Mar 2012).
- [5] C. Weiser, “A Combined Secondary Vertex Based b -Tagging Algorithm in CMS,” CMS Note (25 Jan 2006).
- [6] T. Junk, “Confidence Level Computation for Combining Searches with Small Statistics,” arXiv:hep-ex/9902006v1 (5 Feb 1999).